Navigating Soft Robots through Wireless Heating

Yiwen Song, Mason Zadan, Kushaan Misra, Zefang Li, Jingxian Wang, Carmel Majidi, Swarun Kumar

Carnegie Mellon University

{yiwens2, mzadan, kushaanm, zefangl, cmajidi}@andrew.cmu.edu, {jingxian, swarun}@cmu.edu

Abstract—Recent work on battery-free soft robotics has demonstrated the use of liquid crystal elastomers (LCE) to build shape-changing materials activated by applied external heat. However, sources of heat must typically be in direct field-of-view of the robot (i.e. NIR, laser, and visual light EM sources or convective heats guns), be tethered to an external power supply (i.e. thermoelectric heating or resistive joule heaters), or require a heavy on-board battery that limits mobility and range. This paper presents a novel battery-free soft-robotics platform that can crawl through confined, enclosed, and hard-to-reach spaces (e.g. packages, machinery, pipes, etc.), hidden from view of heating infrastructure. This is achieved through the co-design of a soft robotics platform and integrated soft conductive traces that enable wireless (microwave) heating through remote stimulation. We achieve fast actuation through a careful choice of materials and the overall mechanical structure of the robot to maximize heating efficiency. Further, the robot is actively tracked through enclosed spaces using a mmWave radar to direct heat to its location. We provide a detailed evaluation on the robot's heating efficiency, location-tracking accuracy and crawling speed.

I. INTRODUCTION

Similar to soft creatures such as snails, earthworms, and octopuses, soft robots have the ability to morph their shapes and crawl in different environments [1], [2]. Unlike regular hard robots that are mainly composed of rigid components, soft robots are primarily made of deformable materials and thus have more degrees of freedom for different movements. Specifically, state-of-the-art soft robots are able to mimic the mobility of soft biological organisms [3], [4], [5], [6] and pass through a narrow and confined space without being damaged [7]. Soft robots can be powered using a variety of different actuation methods [8], [5], including shape memory materials like nickel titanium alloy and liquid crystal elastomer (LCE). LCE actuators are emerging as a popular new material architecture for soft robotics due to their complex programmability, versatile manufacturability, and large reversible shape change (*e.g.*, 50% contraction). LCEs exhibit both characteristics of crystalline solid and elastic rubbers through thermally stimulated reversible phase transitions. This transition in material properties leads to a realignment of the polymer chains that induces shape change. Actuation under thermal or EM stimuli is enabled by polymer crosslinking through a variety of techniques including mechanical and UV crosslinking [9], [10], along with the ability to self heal [11]. Using these techniques, researchers have created LCE-based soft robots that are actuated through thermal stimuli to execute tasks such as lifting [12], [13], rolling [14], and walking [15].

However, current methods to stimulate shape-memory responses in LCE actuators rely on cumbersome hardware that greatly limits mobility, especially in tightly confined
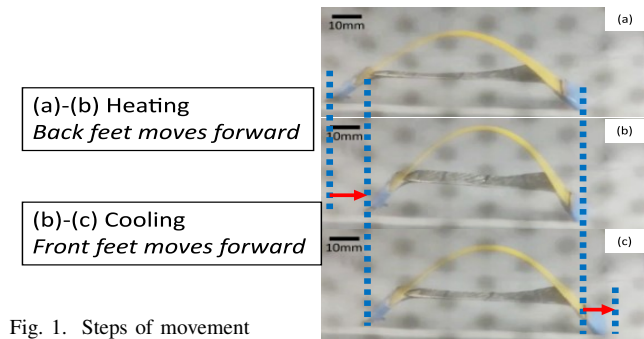

Fig. 1. Steps of movement

spaces. Tethered LCE-based robotic systems can accurately control soft robots for long periods of time [16], [15] but the limiting length and mechanical interference of the wires (e.g. wire tension, entanglement) significantly restricts motion. Challenges with tethered connections can be addressed with wireless circuitry and onboard batteries [17], [18], [19], but this adds bulk that hampers the mobility and adaptability of the system and introduces limitations that arise from battery lives [20], [21]. While optical solutions such as laser [22] and infrared light [23] navigate the soft robot wirelessly, they need direct over-the-air control from the energy source (*i.e.*, a laser emitter) to the soft robot. Indeed, a single piece of paper can easily block most of the transmitted optical energy and result in the failure of the navigation system. These problems hinder soft robotics applications in non-line-of-sight spaces such as behind debris or inside a pipe.

To overcome the challenges with soft robots, we turn to actuator stimulation based on radio-frequency (RF) electro-magnetic (EM) waves. In contrast to heat or light, RF can penetrate through solid barriers, and blockages, and power soft robots that in non-line-of-sight [24]. In this way, we introduce a novel navigation-capable soft robotics platform and associated wireless heating infrastructure that supports robots crawling within confined spaces hidden-from-view relative to heating infrastructure. We co-design LCE patches that effectively absorb the EM waves and a soft robot that is capable of moving under EM actuation. Further, we provide a millimeter-wave (mmWave) radar-based sensing solution to accurately localize the soft robot. The two parts form a closed control loop for the wirelessly-navigated soft robot.

First, we design a soft robot material architecture such that it can be moved through wireless power. In particular, LCE is extremely difficult to heat with EM waves. Recent work [25] reports actuating LCE with 40 seconds of 800 Watts microwave power, which is slow and energy-inefficient compared to tethered and optical actuation, with which only several watts of power is consumed for a few seconds.

Our goal is to achieve an energy conversion efficiency and

response speed that is similar to Joule heating, while enabling heating in a non-line-of-sight scenario. As a solution, we design and embed patterns of direct ink written (DIW) 3D printed eutectic gallium-indium (EGaIn)-silver (Ag) alloy composites[26], [27] inside a sheet of LCE. The use of printable EGaIn-Ag ink allows for the precision manufacturing of flexible conductive traces on the LCE for absorbing EM energy effectively. This leads to fast heating of the conductive traces and LCE, causing shape changes. Through this method, we are able to heat the LCE to 60°C with 10 s of 40 W power. The contraction of the LCE is programmed in by straining the sample above 100% strain and applying UV light for second stage crosslinking to program in the pre-strain [10], [28]. This induces a 50% reversible contract after wireless energy is applied. Then, we carefully design the structure of the soft robot to enable movement. We measure the contraction force that the LCE induces, and then design a backbone-feet structure for the soft robot that helps the LCE to return to its initial state, and enables the soft robot to move, as shown in Figure 1. We also show that the soft robot is able to navigate simple terrains such as slopes and small obstacles.

Second, to navigate and focus energy on the soft robot in an enclosed space, we must continuously monitor the location of the soft robot, which can't be achieved through direct eye or camera monitoring. To resolve the challenge, we make use of mmWave which can penetrate through non-metallic blockages. We develop a mmWave radar-based solution to accurately sense the location of the soft robot, which overcomes the weak soft robot reflected signal and the noise incurred by the reflective surfaces of the metallic enclosure. We use the result of localization to focus EM energy on the soft robot using an energy beamforming formulation, and update the robot location each time the robot moves.

We evaluate the our system inside an EM-enclosed space with 4 antennas and 40 W total emission power. Our platform is enclosed within a Faraday enclosure (either hard metallic or made of flexible metal-based fabrics) to meet FCC regulatory and safety requirements. We evaluate the impact on heating efficiencies of different pattern designs, the accuracy of mmWave localization, and the overall moving speed and performance of the soft robot in different scenarios. Our results show that the selected EGaIn-Silver pattern preserves a heating efficiency of reaching 60°C in 5 s on average. Moreover, our mmWave method provides a maximum localization error of 30 mm for the soft robot inside a pipe. Finally, we evaluate the overall performance of our navigation system and achieve a 0.14 mm/s moving speed, while enabling movement on a slope with a 1/5 gradient.

II. RELATED WORK

Soft robot design: State-of-the-art LCE-based soft robots can be generally classified into two categories: infrared light and laser-actuated and wired Joule heating [9]. Energy from visible and infrared light [23], [29] and ultraviolet light [30] can be used for actuation due to the photothermal effect [31]. With a similar principle, laser-based stimulation [7], [22] usually provides a smaller actuation area that allows for
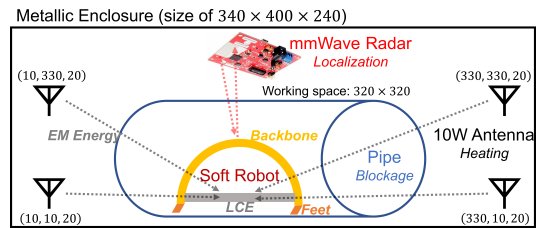

Fig. 2. Structure of the Soft Robot Navigation System

millimeter-scale soft robots. However, optical actuation methods are strictly constrained by the line-of-sight conditions between the emitter and the soft robot, which severely narrows the use cases. Meanwhile, many LCE soft robots are Joule-heated by passing electrical current through serpentine resistive wires [17], [18], [32] or fluidic channels liquid metal [6], [33]. Recent work has also introduced the use of embedded thermoelectric Peltier devices for heating and cooling for LCE actuation [15]. In these cases, Joule and thermoelectrically heated actuation methods require either a wired connection to a power source or a bulky onboard battery, which limits the mobility and range of the soft robot in confined spaces.

EM heating: Although there has been various literature studying the materials and shapes that enable EM heating, theoretical analysis and general model of appropriate materials and patterns is still acknowledged as an under-studied area [34]. Therefore, to design patterns that can be efficiently heated, we adapt a waveguide model, and use an empirical approach to verify how the patterns are heated by EM energy. Previous studies show that microwave heating provides sub-20 mm heating area [35], which is distinguished from visible light and laser, and thus requires us to adapt the design of the soft robot structure accordingly. Metal has long been used for induction heating [36], [37], [38] but there is still a lack of research on the thin metal layer that we use in this study. Metal powder [39], [40], [41] heats quickly but is not resilient to shape change. Ferrite experience magnetic heating [42], [43], but they have low conductivity and would reduce induction heating performance. In this paper, we investigate EM heating of liquid metal silver composites that retains high conductivity when stretched [26], [27], thereby making it a suitable choice for integration in LCE actuators.

Recent papers have introduced the concept of heating soft robots or LCE with electromagnetic energy [25], [44]. However, current approaches need >100 watt power and tens of seconds to heat LCE until 60°C, which is highly energy-inefficient. In this paper, we introduce a new robot design that improves EM heating efficiency and can be navigated using wireless technologies inside of enclosed spaces.

III. OVERVIEW

The system architecture is presented in Figure 2. The EM heating system is set inside of a metallic enclosure to comply with FCC regulations. First, in Sec. IV we design the soft robot to allow it to be efficiently heated by an EM wave. Then in Sec. V, we describe our mmWave radar localization system to track the position of the soft robot, and focus emitting energy from the antennas on the soft robot. Finally, we carry out a detailed evaluation of system performance in Sec. VI.

IV. Soft Robot Design

Soft robot actuation via RF radiation is different from laser, infrared light, or heat guns in nature, since the latter methods use photothermal and conductive heat transfer, respectively. Moreover, microwave actuation requires parts of the soft robotic actuator to resonate with the electromagnetic wave at microwave frequencies so that EM energy is translated into heat energy. These differences result in the requirement of designing a specialized soft robot structure that is compatible with microwave heating for controlled actuation. Major challenges include (1) fabricating soft robots such that they resonate with the 2.4 GHz microwave that we use to actuate and (2) the design soft robot mechanical structure such that it moves efficiently under microwave actuation.

A. EM Resonance Design

Heating Mechanism: An electromagnetic field usually induces heat inside matter through two mechanisms: dielectric heating and induced current. For insulators, the rapidly changing electromagnetic field causes the polar molecules to continuously rotate towards the direction of the electric field. During rotation the molecules collide with each other and emit heat [45], [46], [34]. Previous works apply dielectric heating to heat specifically synthesized LCE at 40°C/sec with 100 Watt power [25]. For conductors, the changing magnetic fields induce current according to Faraday's Law, and the current generates Joule heat [47], [48]. In this paper, we design conductive patterns to make use of Joule heating.

Selection of Conductive Patterns: When EM waves penetrate through highly-conductive materials, they attenuate rapidly, and thus only the surface area of the conductive object absorbs EM energy. This phenomenon is called the skin effect and the depth that the wave can go into is usually approximated as $5\sqrt{\frac{1}{\pi f \mu \sigma}}$, where f is the frequency, μ and σ is the permeability and conductivity of the material, respectively [49]. Due to the skin effect, a full patch of conductive layer cannot be efficiently and uniformly heated since the inner part absorbs much less energy than the edges. The skin effect not only decreases energy efficiency, but also creates non-uniform heating, where the heat concentrates at the edges. Therefore, we design parallel conductive patterns that make full use of the skin effect, as shown in Figure 3(a).

Conductive Material: Since LCE experiences large shape change (*e.g.*, 40% contraction) under actuation, solid-state conductive materials are not applicable as they may bend or break. We thus select eutectic gallium-indium (EGaIn), a type of highly-conductive liquid metal (LM) as the base. To increase conductivity we add silver (Ag) flakes to EGaIn forming regions of AgInGa. To allow for DIW printing, we follow [26] and mix the AgInGa alloy with Polystyrene-block-polyisoprene-block-polystyrene (SIS) thermal-plastic elastomer, which maintains conductivity under 100% strain.

Design of Parallel Patterns: We control three parameters of the parallel conductive traces: width, thickness of the patterns, and spacing between traces. We empirically test different parameters and select the optimal pattern that heats

(a) Conductive pattern   (b) Waveguide
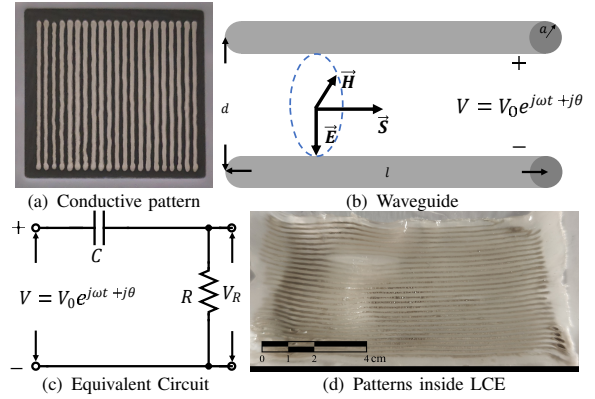
(c) Equivalent Circuit   (d) Patterns inside LCE

Fig. 3. Electrical model of the conductive pattern

the most efficiently in Sec. VI-B. We further model the parallel linear conductive traces inside the EM field as several parallel capacitance waveguides, as shown in Fig. 3(b). The waveguides prevent the EM wave from propagating perpendicular to the patterns. The EM component transmitting through the surface does not create induced current according to Faraday's Law. In this way, we only need to consider the EM component that passes through the parallel spacing between the conductive patterns. The changing magnetic field acts as an AC power supply connected to both ends of the parallel patterns. Therefore, two neighboring conductive lines inside the EM field can be modeled as a parallel strip capacitor connected to an AC power, as shown in Fig. 3(c). The capacitance C is

$$C = \frac{\pi \varepsilon l}{\operatorname{arccosh}\left(\frac{d}{2a}\right)} = \frac{\pi \varepsilon l}{\ln\left(\frac{d}{2a} + \sqrt{\frac{d^2}{4a^2} - 1}\right)} \quad (1)$$

where ε is the air permittivity, l is the line length, d is the line spacing, and a is the line width. The resonate frequency is

$$f_c = \frac{1}{2\pi RC} = \frac{\operatorname{arccosh}\left(0.5 d/a\right)}{2\pi^2 \sigma \varepsilon l^2} . \quad (2)$$

Here, we note that the total resistance $R = 2\sigma l$ is the resistance of two EGaIn-Silver conductive lines, where σ is the resistivity, which is about 2.5 Ω/mm by measurement. We design conductive patterns that resonate with the 2.4 GHz EM field. Then the conductive pattern is enveloped inside the LCE patch as shown in Figure 3(d).

B. Mechanical Design

Prior work has introduced complex and localized actuation through the fabrication of voxelated LCE inducing highly complex actuation, including folding and moving [50], [51]. However, with uni-axial alignment of the LCE along one director of motion as discussed in Sec. IV-C, and the conductive patterns described in the previous section, we are not able to realize the millimeter-level heating accuracy that can be achieved with voxelated LCEs or Joule heating. Therefore, we need to design an appropriate mechanical structure that fits EM heating. We fabricate LCE actuators that contract along one direction when heated and use a backbone design to quicken the de-actuation process of the LCE and enable faster movement. Then we add two feet to induce directional friction so that the soft robot moves along a specific direction,
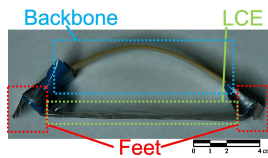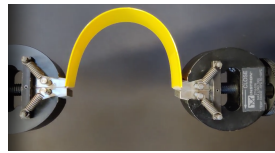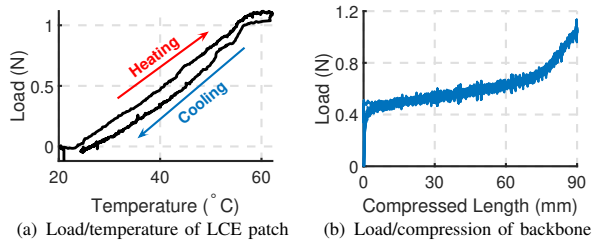
Fig. 4. Robot Structure

Fig. 5. Instron testbed

(a) Load/temperature of LCE patch

(b) Load/compression of backbone

Fig. 6. Mechanical performance of selected materials

Fig. 7. Mounted mmWave radar

Fig. 8. Range-angle profile

and also supports small slopes. The whole structure of the soft robot is presented in Figure 4.

Backbone Design: We use an Instron 2710-11x materials tester to find the induced contraction force of the LCE patch when it is heated and design the backbone structure accordingly. The LCE patch is actuated to 60 degrees using a heat gun and then deactuated. The measured contraction force vs. temperature is in Figure 6(a). We measure the contraction ratio of the LCE patch to be 40%. We also measure the load vs. compressed length of the plastic backbone, and select the compressed length (*i.e.*, 40 mm) that balances the force induced by the LCE patch at 40°C (*i.e.*, 0.5 N).

Feet Design: During the contraction of LCE, it induces same amount of force on both ends. Without a feet design, the robot would only repeat the contraction-releasing process instead of moving towards a specific direction. To enable directional movement, we design feet to induce directional friction between the robot and the contact surface.

C. Fabrication

Conductive Pattern Fabrication: To prepare the conductive ink for printing, we first dissolve the copolymer polystyrene-block-polyisoprene-block-polystyrene (SIS, 14 wt% of styrene; Sigma–Aldrich) into toluene (Sigma–Aldrich) (15 wt% SIS) at 100 °C for 1 h. Then 3.00 g of EGaIn, 1.24 g of silver flakes (SF91; Ames–Goldsmith), and 1.00 g of the SIS solution are mixed. This ink formulation is adapted from [26] and [27]. This composition is then shear mixed for 3 min at 2000 RPM with a planetary centrifugal mixer (AR-100; Thinky Corporation), and transferred to a 10 ml syringe with 27 G Luer tip. With an extrusion-based DIW 3D printer (30M; Hyrel 3D), the conductive pattern can be printed as designed.

LCE Fabrication: We synthesize LCE according to the process given by [10]. First, 5.474 g of 2-methylbenzene-1,4-diylbis4-[3-(acryloyloxy)propoxy]benzoate (RM257; Ambeed, Inc.) is dissolved in 1.7 g of toluene with a heat gun at around 80°C. After cooling down, 0.122 g of crosslinking agent (PETMP; Sigma-Aldrich), 1.538 g of chain extender (EDDET; Sigma-Aldrich) and 0.375 g of photoinitializer (HHMP; Sigma-Aldrich) is mixed in thoroughly at 40°C. Then 0.40 g of catalyst (DPA; Sigma-Aldrich) is added. We
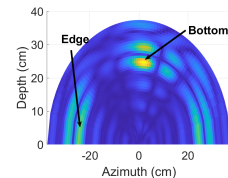
de-gas the mixed solution and pour into the mold with the conductive patterns. After 1.5 h, the LCE is flipped into a deeper mold and the we fill the other side with the same solution. The LCE oligomerizes overnight with an aluminium foil cover. Then, it is put into a vacuum oven under 85°C and 550 mmHg for 24-48 h to fully evaporate the toluene. Finally, the LCE patch is uni-axially strained on a stretcher by >64% length until it's completely transparent, and ultraviolet light at 365 nm is applied for 30 minutes. The fabricated LCE has a capability of contracting 40% by length at the temperature of 65°C.

Robot Assemblage: We fabricate the robot backbone by laser-cutting 0.508 mm yellow PETG plastic sheet (McMaster-Carr) into a bone-shape of 120×25 mm. Following this, the LCE patch is epoxied to the backbone with rubber silicone adhesive (Sil-poxy; Smooth-On). The feet are fabricated by cutting copper sheets into tooth-like patterns, and epoxied to the backbone with Sil-poxy creating directional friction [17].

V. Wireless Robot Navigation

Since we emit power at a low value (40 W) to protect surrounding electronics and to improve energy efficiency, it is important that the EM energy is focused on the robot. However, the soft robot doesn't contain any electronics, so it is not capable of providing any feedback. Therefore, we leverage a mmWave radar (Figure 7) to map the reflective environment and localize the soft robot. We use the information to determine the transmitted signals.

A. Environment Mapping

When a mmWave signal hits a metallic surface, the majority of its energy reflects according to Snell's law of reflection. Therefore, according to the received signal, we can determine the location of reflectors. In Figure 8, we show the range-angle energy distribution generated by 2D Fast Fourier Transform of the received signal [52], which clearly demonstrates the reflectors as peak points. According to the estimation, we can generate a model of the environment as a connection of the reflectors. In our case, the reflectors are aluminum sheets constructing a cube of $340 \times 400 \times 240$ mm^3 with mmWave radar located at the top-middle.

B. Robot Localization and Beamforming

Unlike most large metallic reflectors in the environment, the soft robot is small (of size 85×15 mm^2) and doesn't reflect as much energy, since the backbone is made of plastic and the patterns are mixed with dielectric materials (SIS) to suppress reflection and promote energy absorbance. Moreover, strong reflections of the environment makes energy reflected from the soft robot bounce multiple times inside the enclosure, creating additional noise at different points.

Formulation: To accurately localize the soft robot under these constraints, we develop a combination of signal processing and machine learning methodologies. First, similar to environment mapping, we generate the range-angle profile using 2D-FFT. Instead of using the raw profile, we perform background subtraction, which eliminates most of the environmental reflectors. Let $\boldsymbol{P}$ be the profile with the soft robot, and $\boldsymbol{P}_0$ be the profile of the environment obtained in Sec. V-A, we have the range-angle profile $\boldsymbol{P}_s$ of the soft robot as $\boldsymbol{P}_s = \boldsymbol{P} - \boldsymbol{P}_0 \cdot e^{j\phi}$, where $e^{j\phi}$ is a phase-align term that aligns the phase of $\boldsymbol{P}$ and $\boldsymbol{P}_0$, $j = \sqrt{-1}$ and ϕ is given by the following equation:

$$\phi = \arg\min_\theta \max_{k,l} \left| \boldsymbol{P} - e^{j\theta} \boldsymbol{P}_0 \right|^2_{[k,l]}. \tag{3}$$

However, it is still non-trivial from $\boldsymbol{P}_s$ to infer the accurate location of the soft robot due to strong reflections and error of phase-alignment. Since the inside of the metallic enclosure constitutes a noiseless environment, we develop machine learning techniques to fit from the profile amplitude $|\boldsymbol{P}_s|$ to acquire the location of the soft robot.

Method: Since we want to determine the location of the soft robot as b mm from the origin point, the problem can either be classified as a classification algorithm or a regression algorithm. As a classification algorithm, we let $b \in \{0, 1, 2, \cdots, b_{\max}\} \subset \mathbb{N}$. Therefore the problem evolves as classifying with $|\boldsymbol{P}_s|$ for the most probable value of b. We use support vector machine (SVM) to solve the problem. As a regression algorithm, we adopt both a kernel-ridge regression and a multi-layer perceptron (MLP). The comparison of the three algorithms is shown in Sec. VI-C. Based on performance under cross-validation, we select the 3-layer perceptron as the regressor for the final realization.

Beamforming: To effectively focus EM energy on the soft robot, we need to tune the phase of the transmitting signal of each antenna, which is usually referred to as beamforming. Let τ_i denote the phase of antenna i, $\boldsymbol{S}_i = \boldsymbol{E}_i \times \boldsymbol{H}_i$ denote the energy density provided by antenna i, we want to find τ_i that maximizes the total energy density at the location (x_s, y_s, z_s) of the soft robot, which is given by the following:

$$\max_{\tau_i} \left| \sum_i e^{j\tau_i} \boldsymbol{S}_i(x_s, y_s, z_s) \cdot \boldsymbol{a}_\mathrm{s} \right| \tag{4}$$

where $\boldsymbol{a}_\mathrm{s}$ represents the direction where the parallel patterns are aligned. In practice, we obtain $\boldsymbol{S}_i(x, y, z)$ for all (x, y, z) from the constructed environment in Sec. V-A and CST Studio [53] electromagnetic simulation without the presence of the soft robot. Then we locate the soft robot at (x_s, y_s, z_s) and use Eq. (4) to determine the phase at each antenna. Furthermore, it can also be added to the optimization in Eq. (4) a restriction term to minimize the energy transmitted to sensitive electronics (*e.g.*, the mmWave radar) at location (x_r, y_r, z_r), given by the following optimization:

$$\max_{\tau_i} \left| \sum_i e^{j\tau_i} \boldsymbol{S}_i(x_s, y_s, z_s) \cdot \boldsymbol{a}_\mathrm{s} \right| - \left\| \sum_i e^{j\tau_i} \boldsymbol{S}_i(x_r, y_r, z_r) \right\|_2 \tag{5}$$

which we use for the beamforming phases in evaluation. Note that all $\boldsymbol{E}_i, \boldsymbol{H}_i$ and $\boldsymbol{S}_i$ terms are in phasor form in our previous discussion. The power can be directly taken as magnitude since we only consider the average power.

Index	length (mm)	width (mm)	spacing (mm)	f_c (GHz)
P1	**35**	**1.0**	**2.0**	**2.4616**
P2	35	1.0	2.5	2.9286
P3	35	1.0	3.0	3.2949
P4	25	1.0	2.0	4.8248
P5	15	1.0	2.0	13.402
P6	35	0.5	2.0	3.8569

TABLE I
6 CONDUCTIVE PATTERN PARAMETERS
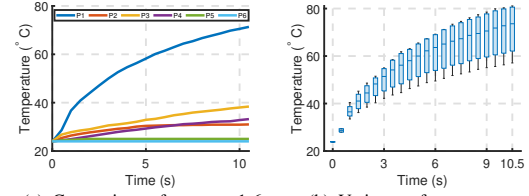
(a) Comparison of patterns 1-6   (b) Variance of temperature

Fig. 9. Temperature vs. Time

VI. EVALUATION

A. Evaluation Setup

Figure 2 demonstrates the geometry of our setup.

Transmitter: We use a setup of 4 RF chains, each with one Ettus USRP X310 software-define radio (SDR), one NXP MHT2012N amplifier, and one RF antenna connected with coaxial cables. The emitting power at each antenna is tuned and maintained at 10 W at the 2.45 GHz ISM center frequency throughout the evaluation, with a total emitting power of 40 W.

Safety: A metallic enclosure is placed outside the heating system to decrease energy leakage to the outer space. We use an aluminum box as the enclosure. One can also switch to RF fabrics [54] which are more flexible and light-weight.

Blockage: We set a blockage from the antenna to the soft robot as a transparent PVC pipe, with an inner radius of 104.0 mm and thickness of 3.0 mm. Throughout the whole evaluation process, the soft robot is maintained inside the pipe. Note that our system is not applicable to metallic blockage since metal can block EM waves easily.

B. Conductive Pattern Heating Efficiency

Evaluation methodology: We first compare 6 different parameters for the conductive patterns shown in Table I, where we adjust the length l, width $2a$, spacing d, and calculate the center frequency f_c. The patterns are then put at 6 different locations along the robot's moving path, and heated wirelessly.

Result: We show the temperature (°C) versus time (s) graph of different patterns in Figure 9(a), captured by a FLIR C3X thermal camera. It can be seen that pattern P1, with resonate frequency laying inside 2.4-2.5 GHz, has the optimal heating efficiency. We further show the bar plot of temperature for pattern P1 in Figure 9(b), where we see that the average time for pattern P1 to reach 60°C is 5 seconds, and time upper bound to 60°C is 9.5 seconds. The result of heating efficiency shows our advantage in EM heating through resonant patterns and beamforming, where we use less energy and time versus prior work that uses hundreds of Watts of power and takes tens of seconds [25]. As a comparison, heating the identical patterns using tethered Joule heating consumes 1.5 W power for each line, yielding a minimum of 10% power efficiency
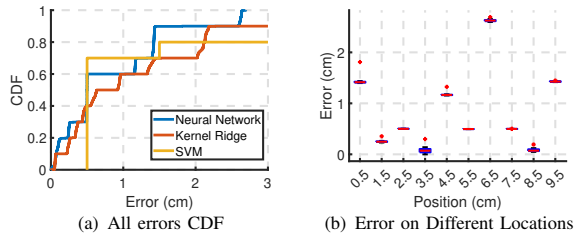
(a) All errors CDF

(b) Error on Different Locations

Fig. 10. mmWave localization accuracy

(a) Actuation process

(b) Cooling process

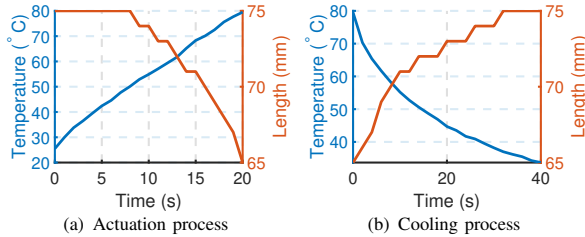Fig. 11. Step-wise analysis of robot movement

(a) w/o slope

(b) w/ slope

Fig. 12. Analysis of robot movement

as we heat 3-4 lines together. Note that the efficiency can be further improved if a larger robot is actuated by RF energy.

C. mmWave-based Robot Localization

Evaluation methodology: We use a TI AWR1843BOOST mmWave radar mounted on top-middle of the enclosure. A pipe is beneath the mmWave radar on the bottom of the enclosure. We first use the mmWave radar to locate reflective surfaces in the environment in Sec. V-A. Then we place the robot inside the pipe, change its location, and record the mmWave radar response. The robot is moved within 0-14.5 cm and mmWave readings are recorded every 0.5 cm. We randomly split data for training and evaluation. The three methodologies we compare are SVM, kernel ridge regression, and a 3-layered fully connected layer (FCL) neural network.

Result: In Figure 10(a), we show the cumulative distribution function (CDF) of error provided by all three algorithms. It can be observed that the 3-layered FCL performs optimally across all three algorithms, achieving <0.4987 cm error in 50% cases, <2.2035 cm error in 90% cases, and <2.6238 cm error in all cases. In comparison, SVM and kernel ridge regression both have long-tail error distribution, which may affect the beamforming performance to some extent. This is because the relationship between the soft robot location and the mmWave radar profile is non-linear and distorted due to highly-reflective surrounding surfaces. We also provide the error bar plot of neural network in Figure 10(b). It can be seen that for all cases the error variance is low, indicating that the neural network is consistent over location change. Our soft robot is of length 8.5 cm. Therefore, the accuracy of 3 cm suffices for beamforming purposes if we target the center of the soft robot.

D. Robot Performance

Step-wise Analysis: Figure 1 shows our robot experiences a 2-step process for each movement. In (a)-(b) the robot contracts and pulls the back feet forward, and in (b)-(c) the robot relaxes and pushes the front feet forward. We first evaluate the time cost for the two steps separately. Figure 11 shows the change in LCE length and temperature during
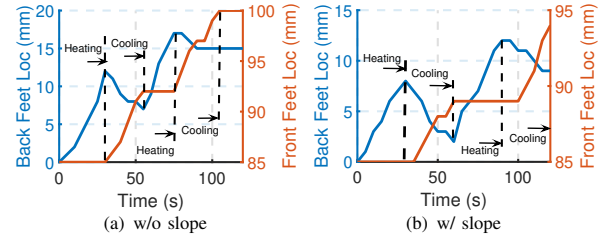
actuation. we observe that it takes ∼20 s for the LCE patch to rise to 80°C and contract 10 mm. The contraction is less than 40% due to the backbone tension, and the temperature rise is lower than raw patterns since LCE is absorbing much heat. Figure 11(b) shows the temperature and length during the cooling process, from which it can be seen that the cooling process is twice more time-consuming than the actuation process. The slow cooling process of LCE is viewed as a general problem in the soft robot community and remains to be solved [15].

Overall Performance: In Figure 12(a) we track the location of the back feet and front feet of our soft robot during the whole moving process. We report the average moving speed of the soft robot to be around 0.14 mm/s inside a pipe, which is comparable to the 0.02-0.3 mm/s speed of LCE-based robots of similar size that are activated using a laser, infrared light, or wired actuation [7], [55]. Note that we observe some slipping at the back feet during the cooling process, which could be addressed through more advanced feet designs. In an ideal case where the back feet does not slip, the theoretic optimal performance could be 0.17 mm/s, given by a 10 mm contraction per actuation and a 60 s actuation-cooling period.

Effect of Slope: Next, we study the effect of terrain slope on the movement of our soft robot. We test the soft robot on pipes with a slope of $1/5$ and track its feet location in Figure 12(b). We see that the slipping of back feet becomes more severe when on a slope, but the soft robot still maintains an average speed of 0.075 mm/s. The experiment shows that our soft robot can navigate slopes without any modification.

VII. CONCLUSION AND FUTURE WORK

This paper introduces a soft robot that can navigate through enclosed spaces using wireless heating. We develop patterned conductive traces integrated into the robot structure to efficiently absorb EM power. We design mmWave-radar based localization techniques to determine the location of the soft robot as it moves, to appropriately focus wireless power on it. Our experiments show that our soft robot can be fully actuated using 40 W transmitting power and navigate on sloped terrains. In the future, we foresee a potential further reduction of emitting power below 10 W with LCE that actuates at lower temperatures [56]. This would not require a metallic enclosure for safety and thus could enable wider use cases. We also leave a more exhaustive robot design study for more complex terrain navigation for future work.

REFERENCES

[1] C. Majidi, "Soft robotics: a perspective—current trends and prospects for the future," *Soft robotics*, vol. 1, no. 1, pp. 5–11, 2014.

[2] M. Wehner, R. L. Truby, D. J. Fitzgerald, B. Mosadegh, G. M. Whitesides, J. A. Lewis, and R. J. Wood, "An integrated design and fabrication strategy for entirely soft, autonomous robots," *nature*, vol. 536, no. 7617, pp. 451–455, 2016.

[3] M.-H. Li and P. Keller, "Artificial muscles based on liquid crystal elastomers," *Philosophical Transactions of the Royal Society A: Mathematical, Physical and Engineering Sciences*, vol. 364, no. 1847, pp. 2763–2777, 2006.

[4] X. Ji, X. Liu, V. Cacucciolo, M. Imboden, Y. Civet, A. El Haitami, S. Cantin, Y. Perriard, and H. Shea, "An autonomous untethered fast soft robotic insect driven by low-voltage dielectric elastomer actuators," *Science Robotics*, vol. 4, no. 37, p. eaaz6451, 2019.

[5] X. Huang, K. Kumar, M. K. Jawed, A. M. Nasab, Z. Ye, W. Shan, and C. Majidi, "Chasing biomimetic locomotion speeds: Creating untethered soft robots with shape memory alloy actuators," *Science Robotics*, vol. 3, no. 25, p. eaau7557, 2018.

[6] B. Ma, C. Xu, L. Cui, C. Zhao, and H. Liu, "Magnetic printing of liquid metal for perceptive soft actuators with embodied intelligence," *ACS Applied Materials & Interfaces*, vol. 13, no. 4, pp. 5574–5582, 2021.

[7] M. Rogóż, K. Dradrach, C. Xuan, and P. Wasylczyk, "A millimeter-scale snail robot based on a light-powered liquid crystal elastomer continuous actuator," *Macromolecular rapid communications*, vol. 40, no. 16, p. 1900279, 2019.

[8] S. Zaidi, M. Maselli, C. Laschi, and M. Cianchetti, "Actuation technologies for soft robot grippers and manipulators: A review," *Current Robotics Reports*, vol. 2, no. 3, pp. 355–369, 2021.

[9] D. Mistry, N. A. Traugutt, K. Yu, and C. M. Yakacki, "Processing and reprocessing liquid crystal elastomer actuators," *Journal of Applied Physics*, vol. 129, no. 13, p. 130901, 2021.

[10] C. Yakacki, M. Saed, D. Nair, T. Gong, S. Reed, and C. Bowman, "Tailorable and programmable liquid-crystalline elastomers using a two-stage thiol–acrylate reaction," *Rsc Advances*, vol. 5, no. 25, pp. 18997–19001, 2015.

[11] Q. He, Z. Wang, Y. Wang, Z. Song, and S. Cai, "Recyclable and self-repairable fluid-driven liquid crystal elastomer actuator," *ACS applied materials & interfaces*, vol. 12, no. 31, pp. 35464–35474, 2020.

[12] Q. He, Z. Wang, Y. Wang, Z. Wang, C. Li, R. Annapooranan, J. Zeng, R. Chen, and S. Cai, "Electrospun liquid crystal elastomer microfiber actuator," *Science Robotics*, vol. 6, no. 57, p. eabi9704, 2021.

[13] A. Kotikian, J. M. Morales, A. Lu, J. Mueller, Z. S. Davidson, J. W. Boley, and J. A. Lewis, "Innervated, self-sensing liquid crystal elastomer actuators with closed loop control," *Advanced Materials*, vol. 33, no. 27, p. 2101814, 2021.

[14] A. Kotikian, C. McMahan, E. C. Davidson, J. M. Muhammad, R. D. Weeks, C. Daraio, and J. A. Lewis, "Untethered soft robotic matter with passive control of shape morphing and propulsion," *Science robotics*, vol. 4, no. 33, p. eaax7044, 2019.

[15] M. Zadan, D. K. Patel, A. P. Sabelhaus, J. Liao, A. Wertz, L. Yao, and C. Majidi, "Liquid crystal elastomer with integrated soft thermoelectrics for shape memory actuation and energy harvesting," *Advanced Materials*, p. 2200857, 2022.

[16] M. J. Ford, C. P. Ambulo, T. A. Kent, E. J. Markvicka, C. Pan, J. Malen, T. H. Ware, and C. Majidi, "A multifunctional shape-morphing elastomer with liquid metal inclusions," *Proceedings of the National Academy of Sciences*, vol. 116, no. 43, pp. 21438–21444, 2019.

[17] J. M. Boothby, J. C. Gagnon, E. McDowell, T. Van Volkenburg, L. Currano, and Z. Xia, "An untethered soft robot based on liquid crystal elastomers," *Soft Robotics*, vol. 9, no. 1, pp. 154–162, 2022.

[18] Q. He, Z. Wang, Y. Wang, A. Minori, M. T. Tolley, and S. Cai, "Electrically controlled liquid crystal elastomer–based soft tubular actuator with multimodal actuation," *Science advances*, vol. 5, no. 10, p. eaax5746, 2019.

[19] M. Wang, Z.-W. Cheng, B. Zuo, X.-M. Chen, S. Huang, and H. Yang, "Liquid crystal elastomer electric locomotives," *ACS Macro Letters*, vol. 9, no. 6, pp. 860–865, 2020.

[20] C. Yuan, D. J. Roach, C. K. Dunn, Q. Mu, X. Kuang, C. M. Yakacki, T. Wang, K. Yu, and H. J. Qi, "3d printed reversible shape changing soft actuators assisted by liquid crystal elastomers," *Soft Matter*, vol. 13, no. 33, pp. 5558–5568, 2017.

[21] H. Lu, Z. Zou, X. Wu, C. Shi, Y. Liu, and J. Xiao, "Biomimetic prosthetic hand enabled by liquid crystal elastomer tendons," *Micromachines*, vol. 12, no. 7, p. 736, 2021.

[22] M. Han, X. Guo, X. Chen, C. Liang, H. Zhao, Q. Zhang, W. Bai, F. Zhang, H. Wei, C. Wu, *et al.*, "Submillimeter-scale multimaterial terrestrial robots," *Science Robotics*, vol. 7, no. 66, p. eabn0602, 2022.

[23] B. Zuo, M. Wang, B.-P. Lin, and H. Yang, "Visible and infrared three-wavelength modulated multi-directional actuators," *Nature communications*, vol. 10, no. 1, pp. 1–11, 2019.

[24] Q. X. Yang, J. Wang, X. Zhang, C. M. Collins, M. B. Smith, H. Liu, X.-H. Zhu, J. T. Vaughan, K. Ugurbil, and W. Chen, "Analysis of wave behavior in lossy dielectric samples at high field," *Magnetic resonance in medicine: an official journal of the international society for magnetic resonance in medicine*, vol. 47, no. 5, pp. 982–989, 2002.

[25] X. Wang, Y. Wang, X. Wang, H. Niu, B. Ridi, J. Shu, X. Fang, C. Li, B. Wang, Y. Gao, *et al.*, "A study of the microwave actuation of a liquid crystalline elastomer," *Soft Matter*, vol. 16, no. 31, pp. 7332–7341, 2020.

[26] P. A. Lopes, D. F. Fernandes, A. F. Silva, D. G. Marques, A. T. de Almeida, C. Majidi, and M. Tavakoli, "Bi-phasic ag–in–ga-embedded elastomer inks for digitally printed, ultra-stretchable, multi-layer electronics," *ACS Applied Materials & Interfaces*, vol. 13, no. 12, pp. 14552–14561, 2021.

[27] W. Zu, Y. Ohm, M. R. Carneiro, M. Vinciguerra, M. Tavakoli, and C. Majidi, "A comparative study of silver microflakes in digitally printable liquid metal embedded elastomer inks for stretchable electronics," *Advanced Materials Technologies*, p. 2200534, 2022.

[28] K. M. Herbert, H. E. Fowler, J. M. McCracken, K. R. Schlafmann, J. A. Koch, and T. J. White, "Synthesis and alignment of liquid crystalline elastomers," *Nature Reviews Materials*, vol. 7, no. 1, pp. 23–38, 2022.

[29] M. Rogóż, H. Zeng, C. Xuan, D. S. Wiersma, and P. Wasylczyk, "Light-driven soft robot mimics caterpillar locomotion in natural scale," *Advanced Optical Materials*, vol. 4, no. 11, pp. 1689–1694, 2016.

[30] A. H. Gelebart, D. Jan Mulder, M. Varga, A. Konya, G. Vantomme, E. Meijer, R. L. Selinger, and D. J. Broer, "Making waves in a photoactive polymer film," *Nature*, vol. 546, no. 7660, pp. 632–636, 2017.

[31] Y. Li, Y. Liu, and D. Luo, "Polarization dependent light-driven liquid crystal elastomer actuators based on photothermal effect," *Advanced Optical Materials*, vol. 9, no. 5, p. 2001861, 2021.

[32] C. Wang, K. Sim, J. Chen, H. Kim, Z. Rao, Y. Li, W. Chen, J. Song, R. Verduzco, and C. Yu, "Soft ultrathin electronics innervated adaptive fully soft robots," *Advanced Materials*, vol. 30, no. 13, p. 1706695, 2018.

[33] T. A. Kent, M. J. Ford, E. J. Markvicka, and C. Majidi, "Soft actuators using liquid crystal elastomers with encapsulated liquid metal joule heaters," *Multifunctional Materials*, vol. 3, no. 2, p. 025003, 2020.

[34] J. Sun, W. Wang, and Q. Yue, "Review on microwave-matter interaction fundamentals and efficient microwave-associated heating strategies," *Materials*, vol. 9, no. 4, p. 231, 2016.

[35] K. P. Nott, J. R. Bows, and M. L. Patrick, "Three-dimensional mri mapping of microwave induced heating patterns," *International journal of food science & technology*, vol. 34, no. 4, pp. 305–315, 1999.

[36] T. Basak, "Influence of various shapes of annular metallic support on microwave heating of 2d cylinders," *Chemical engineering science*, vol. 61, no. 6, pp. 2023–2034, 2006.

[37] T. Basak and A. S. Priya, "Role of metallic and ceramic supports on enhanced microwave heating processes," *Chemical engineering science*, vol. 60, no. 10, pp. 2661–2677, 2005.

[38] K. Ayappa, "Resonant microwave power absorption in slabs," *Journal of Microwave Power and Electromagnetic Energy*, vol. 34, no. 1, pp. 33–41, 1999.

[39] W. L. E. Wong, S. Karthik, and M. Gupta, "Development of high performance mg–al2o3 composites containing al2o3 in submicron length scale using microwave assisted rapid sintering," *Materials Science and technology*, vol. 21, no. 9, pp. 1063–1070, 2005.

[40] S. Chandrasekaran, T. Basak, and S. Ramanathan, "Experimental and theoretical investigation on microwave melting of metals," *Journal of Materials Processing Technology*, vol. 211, no. 3, pp. 482–487, 2011.

[41] S. Singh, D. Gupta, V. Jain, and A. K. Sharma, "Microwave processing of materials and applications in manufacturing industries: a review," *Materials and Manufacturing Processes*, vol. 30, no. 1, pp. 1–29, 2015.

[42] Y. Zhang and Y. Zhai, "Magnetic induction heating of nano-sized ferrite particle," in *advances in induction and microwave heating of mineral and organic materials*, IntechOpen, 2011.

[43] S. Horikoshi, T. Sumi, and N. Serpone, "Unusual effect of the magnetic field component of the microwave radiation on aqueous electrolyte solutions," *Journal of Microwave Power and Electromagnetic Energy*, vol. 46, no. 4, pp. 215–228, 2012.

[44] Y. Li, J. Wu, P. Yang, L. Song, J. Wang, Z. Xing, and J. Zhao, "Multi-degree-of-freedom robots powered and controlled by microwaves," *Advanced Science*, p. 2203305, 2022.

[45] J. Menéndez, A. Arenillas, B. Fidalgo, Y. Fernández, L. Zubizarreta, E. G. Calvo, and J. M. Bermúdez, "Microwave heating processes involving carbon materials," *Fuel Processing Technology*, vol. 91, no. 1, pp. 1–8, 2010.

[46] R. Rosa, P. Veronesi, and C. Leonelli, "A review on combustion synthesis intensification by means of microwave energy," *Chemical Engineering and Processing: Process Intensification*, vol. 71, pp. 2–18, 2013.

[47] Z. Peng, J.-Y. Hwang, and M. Andriese, "Magnetic loss in microwave heating," *Applied Physics Express*, vol. 5, no. 2, p. 027304, 2012.

[48] J. Cheng, R. Roy, and D. Agrawal, "Experimental proof of major role of magnetic field losses in microwave heating of metal and metallic composites," *Journal of Materials Science Letters*, vol. 20, no. 17, pp. 1561–1564, 2001.

[49] B. S. Guru and H. R. Hiziroglu, *Electromagnetic field theory fundamentals*. Cambridge university press, 2009.

[50] T. H. Ware, M. E. McConney, J. J. Wie, V. P. Tondiglia, and T. J. White, "Voxelated liquid crystal elastomers," *Science*, vol. 347, no. 6225, pp. 982–984, 2015.

[51] Y. Guo, J. Zhang, W. Hu, M. T. A. Khan, and M. Sitti, "Shape-programmable liquid crystal elastomer structures with arbitrary three-dimensional director fields and geometries," *Nature communications*, vol. 12, no. 1, pp. 1–9, 2021.

[52] S. Rao, "Introduction to mmwave sensing: Fmcw radars," *Texas Instruments (TI) mmWave Training Series*, pp. 1–11, 2017.

[53] E. S. Solvers and C. Compatibility, "Cst studio suite," 2020.

[54] "Mission darkness titan faraday fabric." https://mosequipment.com/products/titanrf-faraday-fabric, 2022.

[55] M. P. Da Cunha, M. G. Debije, and A. P. Schenning, "Bioinspired light-driven soft robots based on liquid crystal polymers," *Chemical Society Reviews*, vol. 49, no. 18, pp. 6568–6578, 2020.

[56] G. E. Bauman, J. M. McCracken, and T. J. White, "Actuation of liquid crystalline elastomers at or below ambient temperature," *Angewandte Chemie International Edition*, 2022.